Journal of MATERIALS RESEARCH

Article
DOI:10.1557/s43578-022-00821-w

Tuning structural, electrical, linear, and nonlinear optical properties of cadmium zinc telluride quantum dot thin films

Iman A. Mahdy[1,a)], Sara A. Mahmoud[2], Manal A. Mahdy[3]

[1] Physics Department, Faculty of Science, Al-Azhar University (Girls Branch), Cairo 11754, Egypt
[2] Physics Department, School of Sciences and Engineering, The American University in Cairo, New Cairo 11835, Egypt
[3] Solid State Physics Department, National Research Centre, 33 El Buhouth St, Dokki, Giza 12622, Egypt
[a)] Address all correspondence to this author. e-mail: imanmahdy@azhar.edu.eg

Received: 23 September 2022; accepted: 2 November 2022; published online: 14 December 2022

Quantum dots of $Cd_{0.18}Zn_{0.14}Te_{0.68}$ thin films of various thicknesses are deposited on a glass substrate using inert gas condensation and characterized using many techniques. Structural analysis confirms the cubic polymorph of the thin films. The particle size increased from 5.7 to 10.35 nm as the film thickness increased from 10 to 100 nm. Bandgap calculations show two direct allowed transitions, one of which is 1.8 eV for different thicknesses. The other transition changes from the ultra-violet region (3.7 eV) for 10 nm thickness to yellow (2 eV) for 100 nm thickness, depending on the particle size. This result suggests that this material is suitable for use in multiple absorption layers of the same material rather than multilayers of different materials in tandem solar cells. The optical linear and nonlinear parameters highly depend on the particle size. Electrical conductivity shows intrinsic conduction with low activation energies from ambient temperature to 336 K.

Introduction

The use of dual semiconductor materials of zinc telluride and cadmium telluride thin films is crucial in various significant scientific and technological applications, such as solar cells and electronic devices [1–7], light-emitting diodes [8], and photodetectors [9]. This significance is due to their electronic and optical properties, where the dual systems of CdTe and ZnTe have a wide direct bandgap that allows their application as absorbing layers in solar cells [10–13], and they are also characterized by their high absorption coefficient that reaches 10^5 cm^{-1} [12–15].

To produce a significant change in the physical properties of these systems, a tripartite compound of cadmium zinc telluride (CdZnTe) must be achieved by either introducing zinc into CdTe or cadmium into ZnTe, resulting in different properties that make it a key component for various technological applications [16–19]. CdZnTe is considered one of the most significant chalcogenide materials and belongs to the II–VI ternary semiconductor compound. It is a promising candidate for several technological applications, such as in optoelectronics and tandem solar cells [20–22], optoelectronics [23], and radiation detectors [19, 20, 24–26], as it is used as a photoanode for water-splitting applications [27].

Until now, only a few researchers studied the nonlinear optical properties of CdZnTe using the Z-scan method; however, this study spectroscopically calculates both linear and nonlinear optical parameters and discusses them.

Consequently, the main objective of this study is to tune the optical and electrical properties of cadmium zinc telluride nanocrystalline thin films based on their particle size. The inert gas condensation technique was used in this study to grow nanocrystalline $Cd_{0.18}Zn_{0.14}Te_{0.68}$ thin films and inspect their physical properties, including structural, morphological, electrical, linear, and nonlinear optical parameters based on the spectroscopic method.

Results and discussion

Structural and morphological study

Figure 1(a) depicts the recorded EDX spectrum of the prepared cadmium zinc telluride thin film of 100 nm thickness deposited

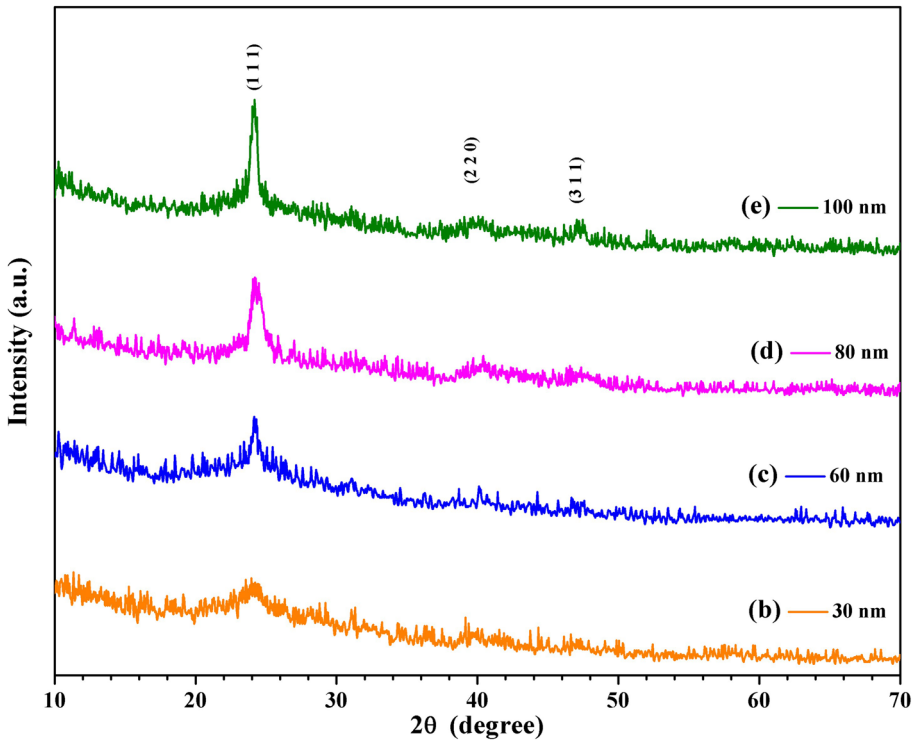

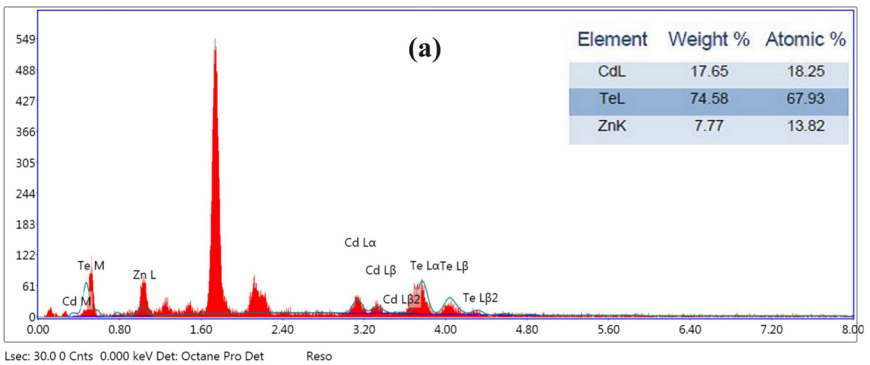

Figure 1: (a) EDX spectrum of $Cd_{0.18}Zn_{0.14}Te_{0.68}$ thin film of 100 nm thickness, and (b–e) the diffraction patterns of grazing incident in-plane X-ray (GIIXD) for $Cd_{0.18}Zn_{0.14}Te_{0.68}$ films of various thicknesses.

on a glass substrate. The peaks of Cd, Zn, and Te are clarified in the spectrum, with atomic ratios are 18.25:13.82:67.93, respectively, as seen in the table inserted in Fig. 1(a). Consequently, the obtained film stoichiometry can be written as $Cd_{0.18}Zn_{0.14}Te_{0.68}$. The excess of Te with 10 at% for antimony telluride material was previously reported by Cullis and Midgley [28], and they discovered a congruence in X-ray diffraction lines for the ICDD standard data and the sample with 10 at.% excess Te.

The phase analysis and internal crystal structure of $Cd_{0.18}Zn_{0.14}Te_{0.68}$ thin films of various thicknesses (30–100 nm) deposited on a cleaned glass substrate were examined using the GIIXD technique. Figure 1(b)–(e) illustrates the X-ray diffraction patterns for all the synthesized films. These patterns confirmed that the films were crystallized in a cubic structure and revealed diffraction lines (111), (220), and (311) that are consistent with the ICDD (Card No. 50-1439) of lattice parameter $a = 6.343$ Å.

Notably, the lower film thickness [30 nm seen in Fig. 1(b)] has a GIIXD pattern with a very low intense diffraction line at the (111) plane, resulting in inaccuracies in calculating its particle size. Therefore, it is predictable that the diffraction line of the plane (111) becomes extremely small or disappears in the case of the lowest film thickness (10 nm). So, the crystallinity and structural nature will be examined from the electron diffraction patterns (EDPs) of HRTEM, which will discuss in the next part. In similar cases, the crystal structure of an extremely small film thickness was studied using HRTEM diffraction patterns, as studied by I. A. Mahdy et al. [29, 30] and M. A. Mahdy et al. [31]. Whereas, as the film thickness is increased, the high

intensive peak becomes sharper, increasing the particle size, as calculated from Scherrer's equation [32]:

$$D = k\lambda/\beta \cdot \cos(\theta).$$

The particle size, D, determined from the most intensive line (111) has values of 8.6, 9.3, and 14.8 nm for film thicknesses of 60, 80, and 100 nm, respectively. This result shows an improvement in the film crystallinity as the film thickness increases [33].

Moreover, the structured nature and particle size of the synthesized $Cd_{0.18}Zn_{0.14}Te_{0.68}$ nanostructured thin films were inspected by HRTEM analysis. The HRTEM images shown in Fig. 2(a) and (d) illustrate the particle distribution, shapes, and sizes of film thicknesses of 10 and 30 nm. Similarly, the particles in Figs. 2(g) and (j) and 3(a) show the micrograph images of film thicknesses of 60, 80, and 100 nm, respectively. All micrograph images in these figures reveal nanoparticle distributions for the synthesized $Cd_{0.18}Zn_{0.14}Te_{0.68}$ thin films. The estimated average particle size is 5.7, 7, 8, 9.1, and 10.35 nm for film thicknesses of 10, 30, 60, 80, and 100 nm, respectively. Some previous reports have mentioned that the CdTe and ZnTe compounds' exciton Bohr radii are 7.3 nm [34, 35] and 4.6 nm [36], respectively. Whereas Lee et al. [37] stated that the estimated Bohr radius of the $Cd_{0.25}Zn_{0.75}Te$ compound is 6 nm. Compared with the X-ray and HRTEM results of our study, the particle radius (2.85–5.17 nm) of the prepared films (10–100 nm in thickness) is smaller and nearly equal to the estimated Bohr radius [37]. In other words, the prepared thin films have strong quantum confinement, indicating their quantum dot (QD) formation. The

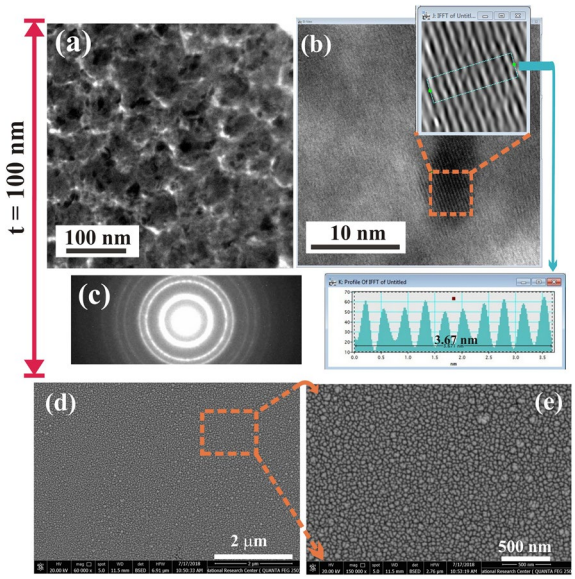

Figure 3: (a–c) HRTEM images, and (d, e) micrograph images of FESEM of the $Cd_{0.18}Zn_{0.14}Te_{0.68}$ nanocrystalline thin films of 100 nm thickness.

EDPs for each film thickness reflect that all thin films showed a crystalline phase, as depicted in Figs. 2(c), (f), (i), and (l) and 3(c). The film's crystallinity was detected by EDP even at a thickness of 10 nm, and it appeared with low crystallinity (30 nm), as depicted in the GIIXD results. In addition, the crystallinity was illustrated in the magnified lattice images for all films that are situated between the orange dashed lines. The d-values of film

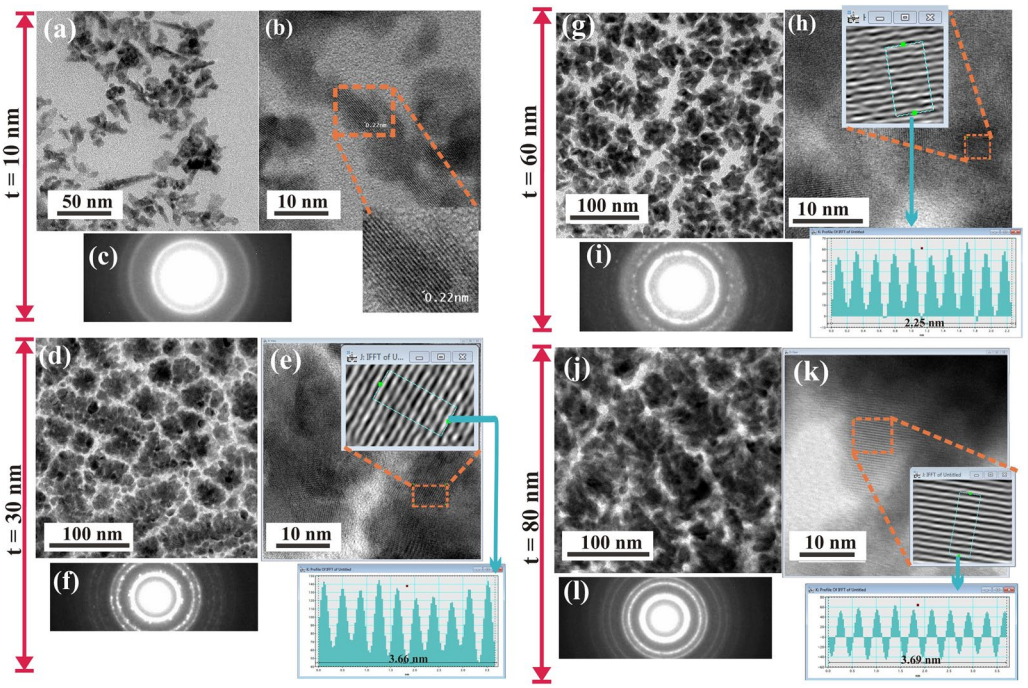

Figure 2: HRTEM images of the $Cd_{0.18}Zn_{0.14}Te_{0.68}$ nanocrystalline thin films, (a–c) 10 nm, (d–f) 30 nm, (g–i) 60 nm, and (j–l) 80 nm.

thicknesses of 30–100 nm were illustrated on the attached lattice maps that are referred to by light blue arrows, as seen in Figs. 2 and 3. The *d*-value for 10 nm thickness is written on the lattice image, as illustrated in Fig. 2(b). The assigned *d*-values were 2.2, 3.66, 2.25, 3.6, and 3.67 Å for film thicknesses of 10, 30, 60, 80, and 100 nm, respectively as depicted in Figs. 2(b), (e), (h), (k) and 3(b). The assigned *d*-values correspond to planes of (111) and (220) of $Cd_{0.18}Zn_{0.14}Te_{0.68}$ cubic structure, which is consistent with reference ICDD Card No. 50-1439 [38] as confirmed by the X-ray result.

The field emission scanning electron microscope (FESEM) images of a thin film of 100 nm thickness as a representative sample were used to identify the surface morphology, as shown in Fig. 3(d) and (e). The micrographs of two magnification scales (2 μm and 500 nm) show good film continuity with a regular grain distribution with very clear boundaries. The grains have a small average size ranging from 17 to 44 nm. These small grains ratified the formation of nanostructured thin films of the chalcogenide semiconductor compound, $Cd_{0.18}Zn_{0.14}Te_{0.68}$.

Optical studies

Figure 4(a) and (b) depicts the recorded optical transmission, *T*, absorption, *A*, and reflection, *R*, spectra for the investigated nanocrystalline thin films of different thicknesses. The values of *T* were inversely proportional to the film thickness, whereby they decreased as the film thickness increased due to the trapping of the incident light in the thicker film than in the thinner one [Fig. 4(a)]. Conversely, the condensed layers of the thicker film increase the *R* values than those for a thinner film [Fig. 4(b)]. The inset panel in Fig. 4(a) represents the absorption spectra of the investigated nanocrystalline films that clarify the shift of the absorption edge toward the higher wavelength as the film thickness increase. These absorption edge shifts reflect the decrease in the thicker film's optical gap value [33]. Moreover, we discovered two steps in the absorption edges for the investigated films in the *A* and *T* spectra, except for the film of 100 nm thickness, which has only a single absorption edge, as seen in Fig. 4(a). All absorption edges were observed in the ultraviolet (UV) and visible wavelength spectral range.

The optical bandgap of the investigated thin films was calculated using the following formula [39, 40];

$$\alpha E = \beta\left(E - E_g\right)^p,$$

where α denotes the absorption coefficient that depends on the transmission and reflection values [40], E_g is the optical gap energy, E signifies an incident photon energy, β represents the bandwidth parameter and p denotes the power factor of transition mode. The E_g calculations verified that the best linear fit refers to the direct allowed transition, i.e., the exponent r equal 1/2.

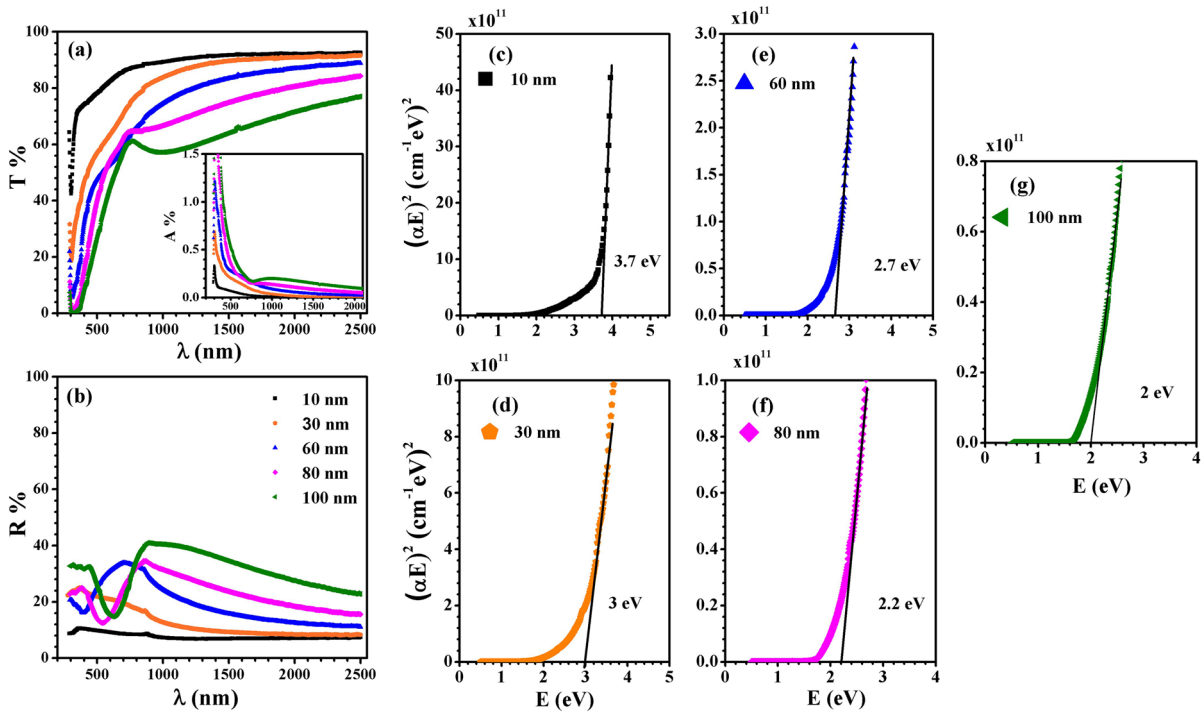

Figure 4: Panel (a) and its inset show the transmission (*T*) and absorption (*A*) spectra, respectively, panel (b) shows the reflection (*R*) spectra, and panels (c–g) represent the graph of $(\alpha E)^2$ versus photon energy *E* for $Cd_{0.18}Zn_{0.14}Te_{0.68}$ nanocrystalline films of different thicknesses, denoting the first optical gap, E_{g1}, transition.

TABLE 1: Obtained values of two transitions of the optical gap (E_{g1} and E_{g2}), dispersion energies (E_{osc} and E_{dis}), oscillator strength, F, both static dielectric constant (ε_s) and refractive index (n_s), ratio of carrier concentration to effective mass ($\frac{N}{m^*}$) and lattice dielectric constant (ε_L), and the of CdZnTe nanocrystalline thin films

	Optical parameters										Conductivity parameters					
Thin film thickness (nm)	E_{g1} (eV)	E_{g2} (eV)	E_{dis} (eV)	E_{osc} (eV)	M_{-1}	M_{-3} $(eV)^{-2}$	F $(eV)^2$	n_s	ε_s	ε_L	$\left(\frac{N}{m^*}\right) \times 10^{37}$ $(kg^{-1}\ m^3)$	Temperature range	W_{dc} (eV)	σ_o $(\Omega\ m)^{-1}$	Temperature range	W_{dc} (eV)	σ_o $(\Omega\ m)^{-1} \times 10^7$
10	3.7	1.8	6.78	4.27	1.59	0.087	28.95	1.61	2.59	2.87	3.2	299–318	0.036	0.00138	334–386	0.693	1.29264
30	3.0	1.8	6.74	3.25	2.07	0.196	21.91	1.75	3.07	3.35	1.9	299–326	0.128	0.01768	336–460	0.820	50.6837
60	2.7	1.8	12.45	3.39	3.67	0.319	42.21	2.16	4.67	5.14	24	299–323	0.173	0.06512	326–473	0.772	10.6112
80	2.2	1.8	18.01	3.47	5.19	0.43	62.51	2.49	6.19	8.22	61	299–336	0.170	0.05175	341–447	0.889	189.661
100	2.0	1.8	21.50	3.11	6.92	0.71	66.86	2.81	7.91	14.39	130	299–322	0.059	0.00063	327–468	0.744	1.97711

The values of activation energy (W_{dc}) for both cycles of heating and cooling for $Cd_{0.18}Zn_{0.14}Te_{0.68}$ QD thin films

The relations between $(\alpha E)^2$ versus photon energy for the synthesized thin films are shown in Figs. 4(c–g) and 5(a–d), revealing two transitions of optical gaps E_{g1} and E_{g2}. The transmission spectra [Fig. 4(a)] and its inset panel of absorption spectra show two distinguishable linear portions for all films, except for the higher film thickness (100 nm), which has only one absorption edge. The two linear portions demonstrate the probability of the simultaneous occurrence of two separate processes of optical transition described by the two optical gaps. The existence of two optical transitions was attributed to the spin–orbit splitting phenomena [41]. Indeed, the two optical gap transitions were reported earlier for chalcogenide thin films of CdSe, CdTe, and Bi_2S_3 [41–43]. The values of the first optical gap, E_{g1}, transition were decreased from the UV absorption (UVA) region (3.7 eV) to the yellow region (2 eV) by increasing the film thickness from 10 to 100 nm, as shown in Fig. 4 and Table 1. However, the value of the second optical gap, E_{g2}, transition (1.8 eV) falls in the red spectral region for films of 10–80 nm thickness, as revealed in Fig. 5. This means that the evaluated optical bandgap values fall in the UVA, violet, blue, green, yellow, and red spectral regions. These results indicate that this substance can be used as a multilayer absorption material rather than using layers of different substances in tandem solar cells.

The complex refractive index ($n^* = n + ik$) is used to describe an important optical property of various materials. From the real ($n = (1 + \sqrt{R})/(1 - \sqrt{R})$) and imaginary ($k = \alpha\lambda/4\pi$) parts of n^*, the optical parameters, such as dispersion and dissipation percentage, of the electromagnetic waves can be determined. Depending on the recorded reflection spectra and calculated absorption coefficient, the refractive index, n, and the extinction coefficient (absorption index), k, were calculated for the investigated films. Figure 5(e, f) depicts the dependence of the calculated n and k values on the film thickness, respectively. This result is consistent with the earlier recorded studies [33, 42, 44, 45] for various semiconductor thin films. Notably, in higher wavelength region (> 900 nm), the refractive index value increase as the film thickness increases [Fig. 5(e)] due to a denser arrangement of atoms, indicating crystallinity improvement.

The refractive index, n, is a key factor for obtaining both linear (X^L) and third-order nonlinear optical susceptibility (X^{NL}) according to the following expressions [46, 47]:

$$X^L = (n^2 - 1)/4\pi,$$

$$X^{NL} = B(X^L)^4,$$

where B denotes a constant (1.7×10^{-10} e.s.u.) and it is almost equal for all materials. The variant of X^L and X^{NL} with photon energy, E, for nanocrystalline $Cd_{0.18}Zn_{0.14}Te_{0.68}$ thin films with different thicknesses is clarified in Fig. 6. From these figures, the X^L and X^{NL} values are affected by the film thickness. Both linear

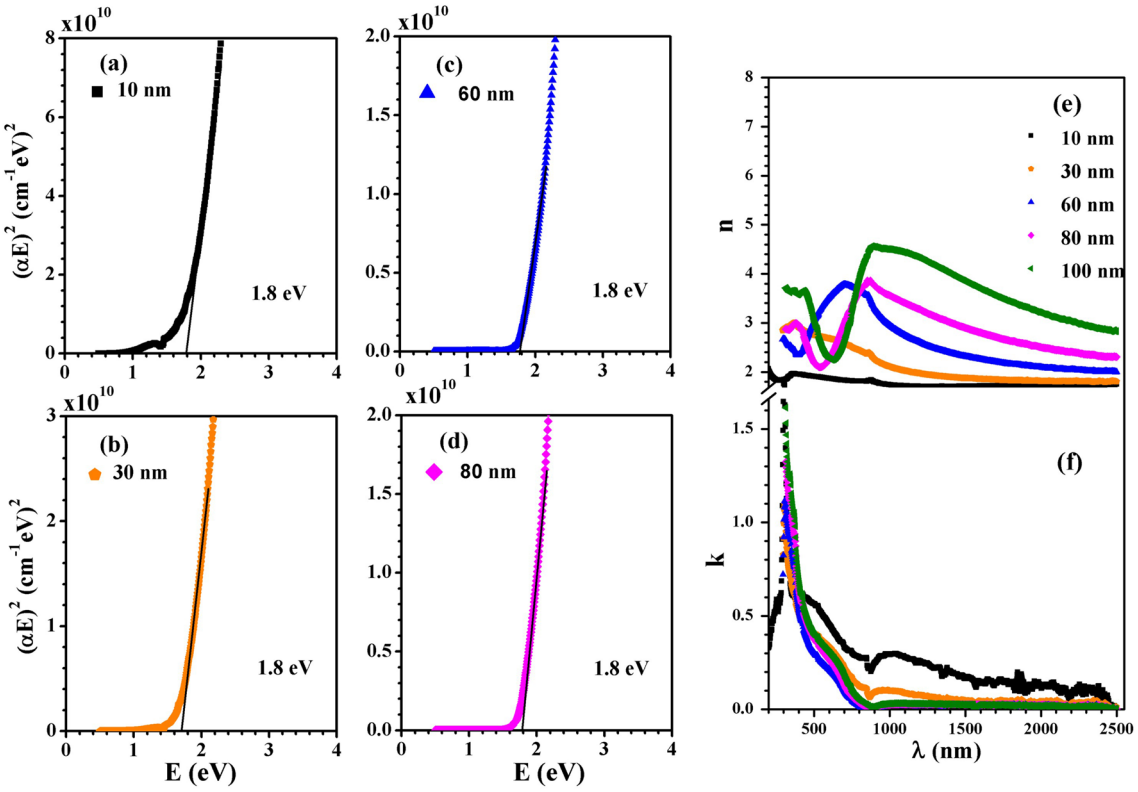

Figure 5: (a–d) The graph of $(\alpha E)^2$ versus photon energy E; denoting the second transition of optical gap, E_{g2}, and (e, f) representative of refractive index, n, and absorption index, k, for nanocrystalline $Cd_{0.18}Zn_{0.14}Te_{0.68}$ thin films of different thicknesses.

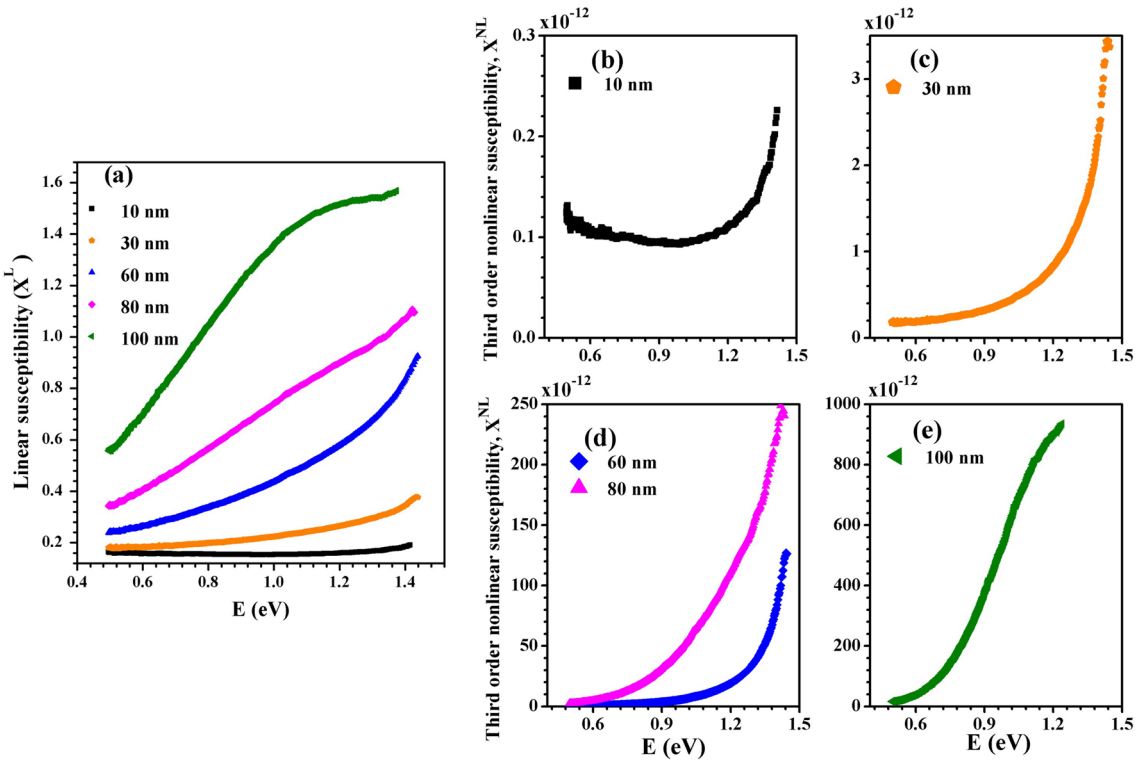

Figure 6: (a) Plot of linear susceptibility, X^L, versus photon energy, E, and (b–e) plot of the nonlinear susceptibility, X^{NL}, versus photon energy, E, for nanocrystalline $Cd_{0.18}Zn_{0.14}Te_{0.68}$ thin films.

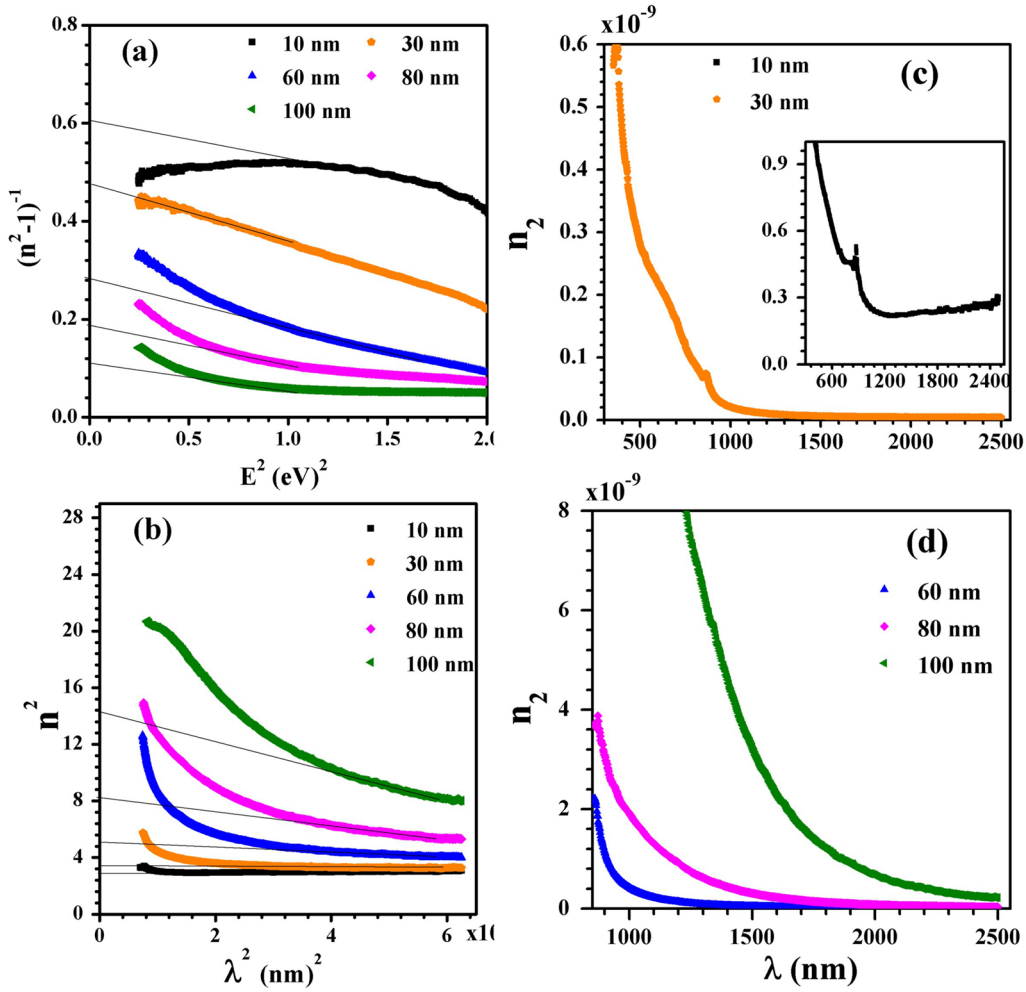

Figure 7: (a) A plot of the inverse of $(n^2-1)^{-1}$ versus E^2, (b) representative of n^2 as a function of λ^2, and (c, d) a plot of nonlinear refractive index vs. wavelength for nanocrystalline $Cd_{0.18}Zn_{0.14}Te_{0.68}$ thin films.

and nonlinear susceptibility is increased with film thickness due to the increased carrier concentration. The increase in carrier concentration with film thickness was previously reported [48, 49].

For wavelengths > 1000 nm [Fig. 5(e)], the n values gradually decrease with increasing wavelength, particularly for higher film thicknesses of 60–100 nm, and are nearly constant for lower thicknesses of 10 and 30 nm. Blow the absorption edge, the n data can be examined using Wemple and DiDiomenico's concept of normal dispersion [50]:

$$n^2 - 1 = E_{dis}E_{osc}/(E_{osc}^2 - E^2),$$

where E_{osc} is the single oscillator energy and E_{dis} denote the dispersion energy. Figure 7(a) shows the relation between $(n^2-1)^{-1}$ and the square value of the photon energy, E^2. The values of E_{osc} and E_{dis} are obtained from the intercept with the $(n^2-1)^{-1}$ axis and the slope of Fig. 7(a), respectively. The obtained values of both oscillator and dispersion energies of the investigated thin films are recorded in Table 1.

Subsequently, important optical parameters that depend on E_{osc} and E_{dis} values can be calculated. These important parameters are the static refractive index ($n_s = \sqrt{1 + E_{dis}/E_{osc}}$) [51–53], oscillator strength ($F = E_{osc}E_{dis}$), and both moments (M_{-1}) and (M_{-3}), which refers to the interband transition strength. The two moments are expressed from relations [53]:

$$E_{osc}^2 = \frac{M_{-1}}{M_{-3}} \quad \text{and} \quad E_{dis}^2 = \frac{M_{-1}^3}{M_{-3}}.$$

The static dielectric constant ($\varepsilon_s = n_s^2$) can be determined when the n_s is calculated. Table 1 lists the calculated values of n_s, ε_s, F, M_{-1}, and M_{-3}, and their values generally increase as the film thickness increases. This result indicates that the increase in film thickness causes crystallization improvement due to denser films. Moreover, the ratio of carrier concentration/effective mass

$\left(\frac{N}{m^*}\right)$ and lattice dielectric constant (ε_L) can be estimated at a higher wavelength from the following relation [54, 55]:

$$n^2 = \varepsilon_L - \left(\frac{e^2 N}{\pi c^2 m^*}\right)\lambda^2,$$

where e and c symbolize the charge of electron and light velocity, respectively. The plot of n^2 versus λ^2 is illustrated in Fig. 7(b), and from its slope and linear extrapolation intercept at $\lambda = 0$, the values of $\left(\frac{N}{m^*}\right)$ and (ε_L) can be assigned, respectively, and recorded in Table 1. The values of ε_L are noticeably large compared with those of ε_s for the investigated films (Table 1). This result reflects the free carrier role in the polarization process inside the films, which is due to the film's exposure to electromagnetic wavelength.

Further, below the optical gap (i.e., absorption edge) region, the nonlinear refractive index (n_2) can be evaluated according to the following formula [46, 56]:

$$n_2 = 12\pi X^{NL}/n_s.$$

Figure 7(c, d) depicts the calculated nonlinear refractive index, n_2, as a function of wavelength. The n_2 behavior showed a rapid decrease in the lower wavelength region, which tends to be constant at a higher wavelength for the films under study. In addition, the values of n_2 are contingent on the thickness of the film.

Some valuable parameters can be computed from the optical data, for example, interband transition strength (J_{CV}) and surface/volume energy loss functions (V_{ELF} and S_{ELF}).

The two parts of the dielectric constant, real ($\varepsilon_r = n^2 - k^2$) and imaginary ($\varepsilon_i = 2nk$), are considered key parameters in determining some significant optical parameters, such as interband transition strength and two-loss functions (surface and volume energy loss).

The material's electronic structure provides information about the density of states for the valence and conduction bands, as well as the electronic transitions from occupied to unoccupied bands [57]. These electronic or interband transitions revealed the optical response in terms of the complex interband transition strength, which is linked to the dielectric constant, as expressed in the following formula [57, 58]:

$$J_{CV} = J_{CV1} + J_{CV2} = \frac{m_e^2}{e^2\hbar^2}\frac{E^2}{8\pi^2}(\varepsilon_i + i\varepsilon_r),$$

where J_{CV1} and J_{CV2} implies the real and imaginary parts of the complex J_{CV}, whereas e and m_e represent the electron charge and mass, respectively.

Figure 8(a, b) shows the interband transitions versus photon energy for nanocrystalline $Cd_{0.18}Zn_{0.14}Te_{0.68}$ thin films. The real part of the interband transition strength increases with the film thickness up to around 4 eV [Fig. 8(a)], whereas the imaginary part increases in low energy up to about 1.5 eV, then it takes an irregular behavior with thickness in the higher energy values

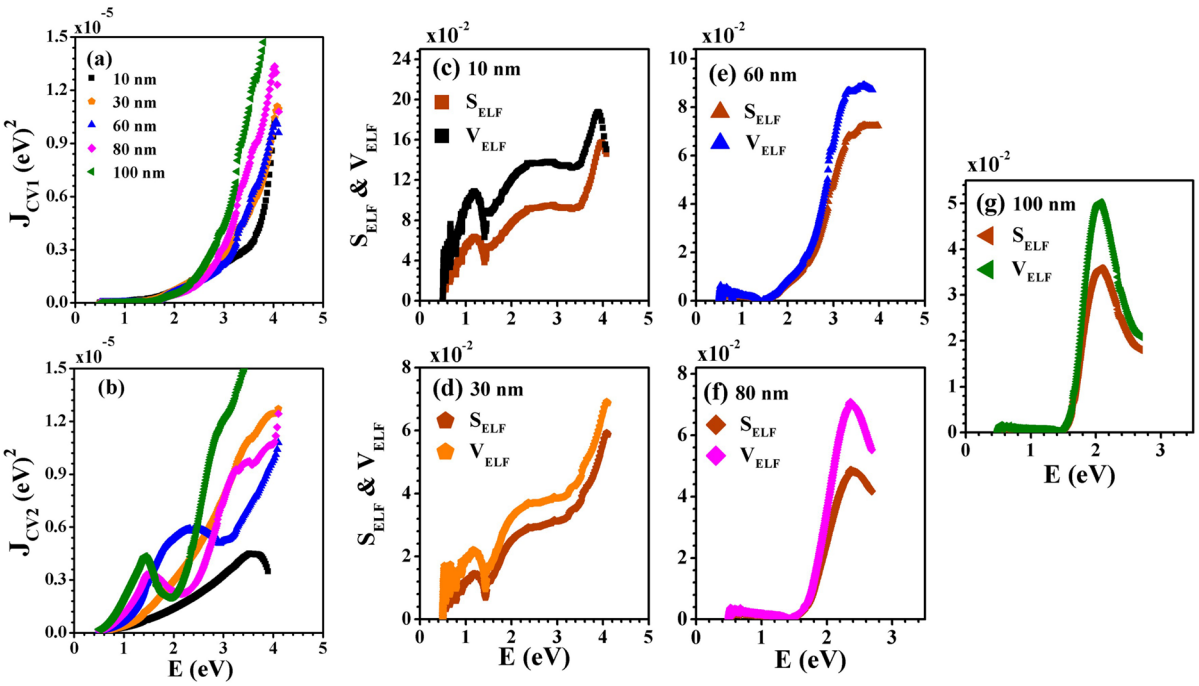

Figure 8: (a, b) Variation of real (J_{CV1}) and imaginary (J_{CV2}) parts of interband transition strength with energy, and (c–g) plot of surface and volume energy loss functions (S_{ELF} and V_{ELF}) vs. energy (E) for $Cd_{0.18}Zn_{0.14}Te_{0.68}$ thin films.

[Fig. 8(b)]. Higher film thicknesses have a higher absorption value, which causes the real and imaginary components of J_{CV} to increase more than lower film thicknesses. Normally, photon energy increases, J_{CV} values increase, indicating that the possibility of materials' electronic transition increases with energy.

In addition, the real part of J_{CV} gives a significant optical response to photon energy at around 1.5 eV, whereas the imaginary part has a response at about 0.7 eV. This result provides strong evidence for the photon absorption increases in the synthesized thin films after around 1.5 and 0.7 eV for the real and imaginary parts of J_{CV}, respectively. The photon absorption results in electronic excitation and causes electron transport from the valence band to the conduction band [58].

The movement of electrons inside the materials is responsible for energy loss, and both functions of volume and surface energy loss were used to determine the probability of losing energy. The two terms V_{ELF} and S_{ELF} depend on the oscillation dielectric functions, ε_r and ε_i, as expressed in the following formulas [59, 60]:

$$V_{ELF} = \frac{\varepsilon_i}{\varepsilon_r^2 + \varepsilon_i^2},$$

$$S_{ELF} = \frac{\varepsilon_i}{(\varepsilon_r + 1)^2 + \varepsilon_i^2}.$$

Figure 8(c–g) depicts the computed V_{ELF} and S_{ELF} of the synthesized nanostructured thin films. The two-loss functions revealed the same behavior for each thickness, and it was observed that V_{ELF} had larger values than S_{ELF} for all films. Both functions increased with a photon energy range of around 1.5–4 eV for the two thicknesses of 10 and 30 nm and from around 1.5–3.3 eV for a 60 nm thickness. However, there are increments from around 1.5–2.3 eV for a thickness of 80 nm and around 1.5–2 eV for a thickness of 100 nm.

The difference in the values of both V_{ELF} and S_{ELF} loss functions may be attributed to the electronic transitions. In other words, the free carriers that traverse through the interior differ from those transferred through the surface because of the film thickness.

Notably, the aforementioned optical results showed that introducing the Zn element into CdTe to attain the CdZnTe materials significantly changes the optical bandgap of their thin films compared with previous studies [31].

Temperature dependence of DC electrical conductivity

Figure 9 depicts the DC electrical conductivity of the as-deposited nanostructured films, which reveals a normal semiconductor behavior. The conductivity slowly increases as the temperature increases from room temperature (300 K) up to around 330 K, and then starts to take a higher rate of increment to 473 K. The electrical conductivity values decrease as the

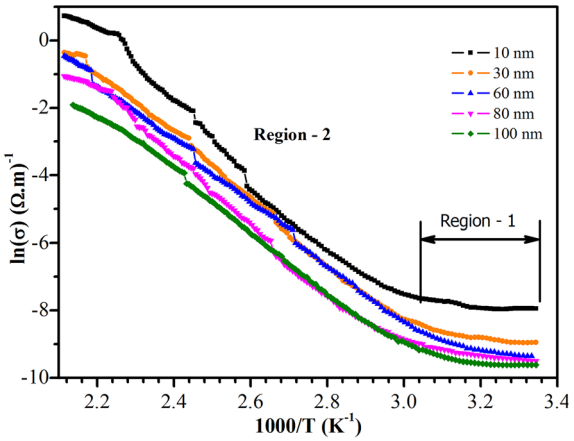

Figure 9: Electrical conductivity as a function of (1000/*T*) of the thin films of different thicknesses of 10–100 nm.

film thickness increases, indicating the growth of particle size (Table 1). In this case, the enhancement in electrical conductivity is attributed to the formation of nanosized particles according to the core–shell model [61]. This result was also confirmed by the previous report of El Zawawi and Mahdy [62] for another nanostructured thin film stoichiometry ($Cd_{0.23}Zn_{0.77}Te$).

The activation energy was evaluated during the heating process using Mott's equation [63, 64]:

$$\sigma(T) = \sigma_o.\exp\left(-\frac{W_{dc}}{KT}\right),$$

where W_{dc} is the activation energy, K denotes Boltzmann's constant, and T is the measured absolute temperature.

At the low-temperature range from room temperature "T_{Room}" to around 336 K, it was observed that the activation energy (W_{dc}) due to extrinsic conduction of impurity carriers increases from 0.036 to 0.17 eV as the film thickness increases from 10 to 80 nm, respectively. However, its value decreases again to 0.059 eV for higher film thickness (100 nm). The activation energy represents around 1.44, 5.12, 6.92, and 6.8 of the KT value, which increases as the film thickness increases from 10 to 80 nm and around 2.35 KT for 100 nm. However, in high-temperature regions "conductivity strong-dependent on temperature" the activation energy is attributed to the intrinsic conduction due to the intrinsic carriers since the activation energy values are close to half of the ionization energies of impurity carriers [65].

Conclusion

Nanocrystals of the ternary chalcogenide semiconductor system of $Cd_{0.18}Zn_{0.14}Te_{0.68}$ thin films were successfully prepared in the form of quantum dots. Their electrical, structural, morphological, linear, and nonlinear optical properties were

investigated in detail. A cubic structure was identified for nanocrystalline thin films via structural investigation. Strong confinement was achieved in the films, as proved by the morphological study and particle size determination. The optical bandgap is successfully tuned by particle size controlled by the film thickness; the particle size increases from 5.7 to 10.35 nm as the film thickness increases from 10 to 100 nm. There were two optical transitions of the films, one reduced from 3.7 eV at 10 nm film thickness to reach 2 eV at 100 nm, including the absorption of different colors for each thickness, whereas the other transition has a fixed value of 1.8 eV that falls in the red region. These variations in the optical bandgap from 3.7 to 1.8 eV cover the UVA and visible spectral light regions. Consequently, the prepared thin films are considered a candidate for multilayer solar cells made of the same material but with layers of varying thicknesses. The determination of linear and nonlinear optical parameters is significantly influenced by the film thickness (i.e., particle size).

Experimental

Five thicknesses of $Cd_{0.18}Zn_{0.14}Te_{0.68}$ were deposited on a glass substrate after undergoing the necessary cleaning process. The deposition process was carried out using the inert gas condensation technique [66]. All deposited films of 10, 30, 60, 80, and 100 nm thickness were inspected using different techniques. The grazing incident in-plane X-ray diffraction (GIIXD, Empyrean Panalytical instrument—Netherlands) was used to determine the phase purity. The shape and particle size were determined using a high-resolution transmission electron microscope (HRTEM) Joel-1230, Japan. A FESEM (Quanta FEG 250, Czech Republic) was used to study the surface morphology and energy dispersive X-ray (EDX) analysis for composition determination of the highest film thickness. Optical measurements were collected at ambient temperature using a spectrophotometer [JASCO V-570, Japan]. The electrical conductivity was measured during isochronal heating from room temperature up to 473 K in an evacuated system (0.1 mbar).

Acknowledgments

This work was not supported by any particular grant from funding organizations.

Author contributions

IAM: Resources, Conceptualization, Investigation, Analysis, Writing, Review, Editing, and Project Administration. SAM: Formal Analysis. MAM: Resources, Conceptualization, Investigation, Analysis, Writing Original Draft, Review, and Editing.

Funding

Open access funding provided by The Science, Technology & Innovation Funding Authority (STDF) in cooperation with The Egyptian Knowledge Bank (EKB).

Data availability

The datasets generated during and/or analyzed during the current study are available on request from the corresponding author.

Declarations

Conflict of interest The authors declare that they have no known competing financial interests or personal relationships that could have appeared to influence the work reported in this paper.

References

1. G. Kartopu, D. Turkay, C. Ozcan, W. Hadibrata, P. Aurang, S. Yerci, H.E. Unalan, V. Barrioz, Y. Qu, L. Bowen, A.K. Gürlek, P. Maiello, R. Turan, S.J.C. Irvine, Photovoltaic performance of CdS/CdTe junctions on ZnO nanorod arrays. Sol. Energy Mater. Sol. Cells **176**, 100–108 (2018). https://doi.org/10.1016/j.solmat.2017.11.036
2. P. Chamola, P. Mittal, Impact of ZnTe, SbZnTe and SnZnTe absorber materials for multi-layered solar cell: parametric extraction and layer wise internal analysis. Optik **224**, 165626 (2020). https://doi.org/10.1016/j.ijleo.2020.165626
3. S. Chander, M.S. Dhaka, Influence of thickness on physical properties of vacuum evaporated polycrystalline CdTe thin films for solar cell applications. Physica E **76**, 52–59 (2016). https://doi.org/10.1016/j.physe.2015.09.044
4. E. Akbarnejad, M. Ghoranneviss, S. Mohajerzadeh, M.R. Hantehzadeh, E. Asl Soleimani, Optical absorption enhancement of CdTe nanostructures by low-energy nitrogen ion bombardment.

J. Phys. D **49**, 075301 (2016). https://doi.org/10.1088/0022-3727/49/7/075301

5. O.I. Olusola, M.L. Madugu, N.A. Abdul-Manaf, I.M. Dharmadasa, Growth and characterisation of n- and p-type ZnTe thin films for applications in electronic devices. Curr. Appl. Phys. **16**, 120–130 (2016). https://doi.org/10.1016/j.cap.2015.11.008
6. F. Fauzi, D.G. Diso, O.K. Echendu, V. Patel, Y. Purandare, R. Burton, I.M. Dharmadasa, Development of ZnTe layers using electrochemical technique for applications in thin film solar cells. Semicond. Sci. Technol. **28**, 045005 (2013). https://doi.org/10.1088/0268-1242/28/4/045005
7. B.H. AlMaiyaly, B.H. Hussein, A.H. Shaban, Fabrication and characterization study of ZnTe/n-Si heterojunction solar cell application. J. Phys. Conf. Ser. **1003**, 012084 (2018). https://doi.org/10.1088/1742-6596/1003/1/012084
8. T. Tanaka, K. Saito, M. Nishio, Q. Guo, H. Ogawa, Enhanced light output from ZnTe light emitting diodes by utilizing thin film structure. Appl. Phys. Express **2**, 122101 (2009). https://doi.org/10.1143/APEX.2.122101
9. H. Hassun, Study of Photodetector Properties ZnTe:Al/Si Prepared by Thermal Evaporation, PhD Thesis, University of Baghdad, Iraq, 2017
10. H. Bayad, A. El Manouni, B. Marí, Y.H. Khattak, S. Ullah, F. Baig, Influence of P^+-ZnTe back surface contact on photovoltaic performance of ZnTe based solar cells. Opt. Quantum Electron. **50**, 259 (2018). https://doi.org/10.1007/s11082-018-1530-0
11. K. Seshan, *Handbook of Thin Film Deposition*, 3rd edn. (Elsevier, London, 2012). https://doi.org/10.1016/C2009-0-64359-2
12. O. Skhouni, A. El Manouni, B. Mari, Hanif Ullah, Numerical study of the influence of ZnTe thickness on CdS/ZnTe solar cell performance. Eur. Phys. J. Appl. Phys. **74**, 24602 (2016). https://doi.org/10.1051/epjap/2015150365
13. D.K. Shah, K.C. Devendra, M. Muddassir, M.S. Akhtar, C.Y. Kim, O.-B. Yang, A simulation approach for investigating the performances of cadmium telluride solar cells using doping concentrations, carrier lifetimes, thickness of layers, and band gaps. Sol. Energy **216**, 259–265 (2021). https://doi.org/10.1016/j.solener.2020.12.070
14. Md. Muin Uddin, Design and Analysis of a High Efficiency and Ultrathin $Zn_xCd_{1-x}S$/ZnCdTe Solar Cell, MSc Thesis, MUET, Bangladesh, 2015
15. O. Oklobia, G. Kartopu, S.J.C. Irvine, Properties of arsenic-doped ZnTe thin films as a back contact for CdTe solar cells. Materials **12**, 3706 (2019). https://doi.org/10.3390/ma12223706
16. A. Kathalingam, S. Valanarasu, S. Ramesh, H.S. Kim, H.-S. Kim, Photoelectrochemical solar cell study of electrochemically synthesized $Cd_{1-x}Zn_xTe$ thin films. Sol. Energy **224**, 923–929 (2021). https://doi.org/10.1016/j.solener.2021.06.065
17. K. Bashir, N. Mehboob, A. Ali, A. Zaman, M. Ashraf, M. Lal, K. Althubeiti, M. Mushtaq, Fabrication and characterization of $Cd_{1-x}Zn_xTe$ thin films for photovoltaic applications. Mater. Lett. **304**, 130737 (2021). https://doi.org/10.1016/j.matlet.2021.130737
18. E. Yilmaz, An investigation of CdZnTe thin films for photovoltaics. Energy Sources A **34**, 332–335 (2012). https://doi.org/10.1080/15567036.2010.490824
19. T. Schulman, Si, CdTe and CdZnTe Radiation Detectors for Imaging Applications. PhD Thesis, University of Helsinki, Finland, 2006
20. N.A. Shah, W. Mahmood, M. Abbas, N. Nazar, A.H. Khosa, A. Zeb, A. Malik, The synthesis of CdZnTe semiconductor thin films for tandem solar cells. RSC Adv. **11**, 39940 (2021). https://doi.org/10.1039/D1RA07755D
21. S. Chander, M.S. Dhaka, Effect of thickness on physical properties of electron beam vacuum evaporated CdZnTe thin films for tandem solar cells. Physica E **84**, 112–117 (2016). https://doi.org/10.1016/j.physe.2016.05.045
22. S. Chander, M.S. Dhaka, Optimization of structural, optical and electrical properties of CdZnTe thin films with the application of thermal treatment. Mater. Lett. **182**, 98–101 (2016). https://doi.org/10.1016/j.matlet.2016.06.093
23. M. Fiederle, Narrow-gap II–VI compounds for optoelectronic and electromagnetic applications. Cryst. Res. Technol. **34**(2), 196–196 (1999). https://doi.org/10.1002/(SICI)1521-4079(199902)34:2%3c196::AID-CRAT196%3e3.0.CO;2-E
24. J. Huang, Q. Gu, F. Yang, K. Tang, S. Gou, Z. Zhang, Y. Shen, J. Zhang, L. Wang, Y. Lu, Growth and properties of CdZnTe films on different substrates. Surf. Coat. Technol. **364**, 444–448 (2019). https://doi.org/10.1016/j.surfcoat.2018.10.083
25. U.N. Roy, R.M. Mundle, G.S. Camarda, Y. Cui, R. Gul, A. Hossain, G. Yang, A.K. Pradhan, R.B. James, Novel ZnO: Al contacts to CdZnTe for X- and gamma-ray detectors. Sci. Rep. **6**, 26384 (2016). https://doi.org/10.1038/srep26384
26. X. Gao, H. Sun, D. Yang, P. Wangyang, C. Zhang, X. Zhu, Large-area CdZnTe thick film based array X-ray detector. Vacuum **183**, 109855 (2021). https://doi.org/10.1016/j.vacuum.2020.109855
27. J. Bie, S. Wang, Y. Guan, X. Zhang, Y. Sun, C. Sun, K. Tang, J. Huang, M. Cao, J. Ling, K. Tan, Y. Shen, L. Wang, Close-spaced sublimation of CdZnTe: In films for solar energy water splitting. Energy Fuels **35**, 8234–8245 (2021). https://doi.org/10.1021/acs.energyfuels.1c00356
28. A.G. Cullis, P.A. Midgley, *Microscopy of Semiconducting Materials*, 1st ed. (2003). https://doi.org/10.1201/9781351074636
29. I.A. Mahdy, M.A. Mahdy, S.M. El Sheikh, Study of the structural, electrical and optical properties of Ge–Pb–Te nanocrystals. Eur. Phys. J. D **70**, 264 (2016). https://doi.org/10.1140/epjd/e2016-70307-2
30. I.A. Mahdy, E.A. Mahmoud, M.A. Mahdy, Tin telluride quantum dot thin films: size dependent structural, optical and electrical properties. Mater. Sci. Semicond. Process. **121**, 105398 (2021). https://doi.org/10.1016/j.mssp.2020.105398

31. M.A. Mahdy, E.A. Mahmoud, I.A. Mahdy, Linear and nonlinear optical response dependency on the crystallite size of CdTe and its structural properties. Surf. Interfaces **23**, 100974 (2021). https://doi.org/10.1016/j.surfin.2021.100974
32. B.D. Cullitty, *Elements of X-Ray Diffraction*, 2nd edn. (Addison Wesley, Boston, 1978)
33. R. Zarei Moghadam, M.H. Ehsani, H. Rezagholipour Dizaji, M.R. Sazide, Thickness dependence of structural and optical properties of CdTe films. Iran. J. Mater. Sci. Eng. **15**, 21–31 (2018). https://doi.org/10.22068/ijmse.l5.3.21
34. T. Rajh, O.I. Micic, A.J. Nozik, Synthesis and characterization of surface-modified colloidal CdTe quantum dots. J. Phys. Chem. **97**, 11999–12003 (1993). https://doi.org/10.1021/j100148a026
35. S.M. Ma, J.T. Seo, W. Yu, Q. Yang, B. Tabibi, D. Temple, N. Min, S.S. Jung, W.J. Kim, Ultrafast time-resolved DFWM of CdTe quantum dots in toluene. In *International Symposium on Advanced Nanodevices and Nanotechnology*, 2008, p. 012025 (2008)
36. H. Ji, Properties of Type-II ZnTe/ZnSe Submonolayer Quantum Dots Studied via Excitonic Aharonov–Bohm Effect and Polarized Optical Spectroscopy, PhD Thesis, Graduate Center, City University of New York, 2016
37. D. Lee, J.E. Zucker, A.M. Johnson, R.D. Feldman, R.F. Austin, Room temperature excitonic saturation in CdZnTe/ZnTe quantum wells. Appl. Phys. Lett. **57**, 1132 (1990). https://doi.org/10.1063/1.103513
38. JCPDS-International Centre for Diffraction Data, *Card Number (50-1439)* (JCPDS-International Centre for Diffraction Data, 2001)
39. J.I. Pankove, *Optical Processes in Semiconductors* (Prentice-Hall Inc, Englewood Cliffs, 1971)
40. J. Tauc, *Amorphous and Liquid Semiconductors* (Plenum, London, 1974)
41. M.A. Zubair, M.T. Chowdhury, M.S. Bashar, M.A. Sami, M.F. Islam, Thickness dependent correlation between structural and optical properties of textured CdSe thin film. AIP Adv. **9**, 045123 (2019). https://doi.org/10.1063/1.5096594
42. S. Lalitha, R. Sathyamoorthy, S. Senthilarasu, A. Subbarayan, K. Natarajan, Characterization of CdTe thin film dependence of structural and optical properties on temperature and thickness. Sol. Energy Mater. Sol. Cells **82**, 187–199 (2004). https://doi.org/10.1016/j.solmat.2004.01.017
43. R.S. Mane, J.D. Desai, O.-S. Joo, S.-H. Han, Surface morphology and optical studies of non-aqueous Bi_2S_3 thin films. Int. J. Electrochem. Sci. **2**, 141–148 (2007)
44. M.A. Mahdy, I.A. Mahdy, E.A. Mahmoud, Structural and optical properties of PbSe nanostructure thin films prepared by inert gas condensation. Physica E **59**, 117–123 (2014). https://doi.org/10.1016/j.physe.2014.01.009
45. M.F. Hasaneen, Z.A. Alrowaili, W.S. Mohamed, Structure and optical properties of polycrystalline ZnSe thin films: validity of Swanepol's approach for calculating the optical parameters. Mater. Res. Express **7**, 016422 (2020). https://doi.org/10.1088/2053-1591/ab6779
46. M.J. Weber, *Handbook of Optical Materials* (CRC Press, Boca Raton, 2003)
47. A.Q. Abdullah, Surface and volume energy loss, optical conductivity of Rhodamine 6G dye (R6G). Chem. Mater. Res. **3**, 56–64 (2013)
48. C.-C. Kuo, C.-C. Liu, S.-C. He, J.-T. Chang, J.-L. He, The influences of thickness on the optical and electrical properties of dual-ion-beam sputtering-deposited molybdenum-doped zinc oxide layer. J. Nanomater. **2011**, 140697 (2011). https://doi.org/10.1155/2011/140697
49. A.P. Amalathas, M.M. Alkaisi, Effects of film thickness and sputtering power on properties of ITO thin films deposited by RF magnetron sputtering without oxygen. J. Mater. Sci. Mater. Electron. **27**, 11064–11071 (2016). https://doi.org/10.1007/s10854-016-5223-9
50. S.H. Wemple, M. Didomenico, Behavior of the electronic dielectric constant in covalent and ionic materials. Phys. Rev. B **3**, 1338–1351 (1971). https://doi.org/10.1103/PhysRevB.3.1338
51. S. Venkatajalapathi, K. Ramesh, K.R. Murali, Pulse electrodeposited $AgInS_2$ films. J. Mater. Sci. Mater. Electron. **25**, 3332–3336 (2014). https://doi.org/10.1007/s10854-014-2022-z
52. N. A. Bakr, A. M. Funde, V. S. Waman, M. M. Kamble, R. R. Hawaldar, D. P. Amalnerkar, S. W. Gosavi, S. R. Jadkar, Determination of the optical parameters of a-Si: H thin films deposited by hot wire-chemical vapour deposition technique using transmission spectrum only. J. Phys. **76**, 519–531 (2011). https://doi.org/10.1007/s12043-011-0024-4
53. S.H. Wemple, Refractive-index behavior of amorphous semiconductors and glasses. Phys. Rev. B **7**, 3767–3777 (1973). https://doi.org/10.1103/PhysRevB.7.3767
54. E.D. Palik, *Handbook of Optical Constants of Solids* (Academic, New York, 1985)
55. G.A. Kumar, J. Thomas, N. George, B.A. Kumar, P. Radhakrishnan, V.P.N. Nampoori, C.P.G. Vallabhan, Optical absorption studies of free (H_2Pc) and rare earth (RePc) phthalocyanine doped borate glasses. Phys. Chem. Glasses **41**, 89–93 (2000)
56. R. Adair, L.L. Chase, S.A. Payne, Nonlinear refractive index of optical crystals. Phys. Rev. B **39**, 3337–3350 (1989). https://doi.org/10.1103/PhysRevB.39.3337
57. R.H. French, Origins and applications of London dispersion forces and Hamaker constants in ceramics. J. Am. Ceram. Soc. **83**, 2117–2146 (2000). https://doi.org/10.1111/j.1151-2916.2000.tb01527.x
58. G.L. Tan, L.K. Denoyer, R.H. French, M.J. Guittetd, M. Gautier-Soyerd, Kramers–Kronig transform for the surface energy loss function. J. Electron Spectrosc. Relat. Phenom. **142**, 97–103 (2004). https://doi.org/10.1016/j.elspec.2004.09.002

59. K. Anshu, A. Sharma, Study of Se based quaternary Se–Pb–(Bi, Te) chalcogenide thin films for their linear and nonlinear optical properties. Optik **127**, 48–54 (2016). https://doi.org/10.1016/j.ijleo.2015.09.228
60. S. Sarkar, N.S. Das, K.K. Chattopadhyay, Optical constants, dispersion energy parameters and dielectric properties of ultra-smooth nanocrystalline $BiVO_4$ thin films prepared by RF-magnetron sputtering. Solid State Sci. **33**, 58–66 (2014). https://doi.org/10.1016/j.solidstatesciences.2014.04.008
61. T.K. Pietrzak, J.E. Garbarczyk, I. Gorzkowska, M. Wasiucionek, J.L. Nowinski, S. Gierlotka, P. Jozwiak, Correlation between electrical properties and microstructure of nanocrystallized V_2O_5–P_2O_5 glasses. J. Power Sources **194**, 73–80 (2009). https://doi.org/10.1016/j.jpowsour.2009.02.031
62. I.K. El Zawawi, M.A. Mahdy, Air-stable $Cd_{0.23}Zn_{0.77}Te$ nanostructure thin films. J. Mater. Sci. Mater. Electron. **26**, 1950–1958 (2015). https://doi.org/10.1007/s10854-014-2634-3
63. N.F. Mott, E.A. Davis, *Electronic Processes in Non-crystalline Materials* (Clarendon Press, Oxford, 1971)
64. M.A. Mahdy, I.A. Mahdy, I.K. El Zawawi, Characterization of $Pb_{24}Te_{76}$ quantum dot thin film synthesized by inert gas condensation. Spectrochim. Acta A **134**, 302–309 (2015). https://doi.org/10.1016/j.saa.2014.06.055
65. G. Yepifanov, *Physical Principles of Microelectronics* (Mir Publisher, Moscow, 1974)
66. I.K. El Zawawi, M.A. Mahdy, Synthesis and characterization of low particle size nanocrystalline SnSe thin films. J. Mater. Sci. Mater. Electron. **24**, 2106–2111 (2013). https://doi.org/10.1007/s10854-013-1065-x